Polarization sensitive photodetector based on quasi-1D ZrSe₃

Xingang Wang[1, 4], Tao Xiong[2], Kaiyao Xin[2, 3], Juehan Yang[2], Yueyang Liu[2], Zeping Zhao[1, †], Jianguo Liu[1, †], and Zhongming Wei[2, 3, †]

[1]The State Key Laboratory on Integrated Optoelectronics, Institute of Semiconductors, Chinese Academy of Sciences, Beijing 100083, China

[2]State Key Laboratory of Superlattices and Microstructures, Institute of Semiconductors, Chinese Academy of Sciences, Beijing 100083, China

[3]Sino-Danish Center for Education and Research, Sino-Danish College University of Chinese Academy of Sciences, Beijing 100049, China

[4]Center of Materials Science and Optoelectronics Engineering, University of Chinese Academy of Sciences, Beijing 100049, China

Abstract: The in-plane anisotropy of transition metal trichalcogenides (MX₃) has a significant impact on the molding of materials and MX₃ is a perfect choice for polarized photodetectors. In this study, the crystal structure, optical and optoelectronic anisotropy of one kind of quasi-one-dimensional (1D) semiconductors, ZrSe₃, are systematically investigated through experiments and theoretical studies. The ZrSe₃-based photodetector shows impressive wide spectral response from ultraviolet (UV) to near infrared (NIR) and exhibits great optoelectrical properties with photoresponsivity of 11.9 mA·W⁻¹ and detectivity of ~10⁶ at 532 nm. Moreover, the dichroic ratio of ZrSe₃-based polarized photodetector is around 1.1 at 808 nm. This study suggests that ZrSe₃ has potential in optoelectronic applications and polarization detectors.

Key words: quasi-1D; ZrSe₃; polarization-sensitive

1. Introduction

In recent years, transition metal dichalcogenides (TMDCs) have gained attention due to their tunable optical, optoelectrical and physiochemical properties[1] that originate from quantum confinement effects and low dimensionality[2–12]. Meanwhile, layered semiconductor materials and their heterojunctions have potential applications in constructing the next generation of optoelectronic devices[13–16]. As one member in the TMDCs family, transition metal trichalcogenides (MX₃) have been a source of attention for many years. The weak van der Waals amalgamated structures of MX₃ constitute a distinct family of compounds, where M represents the metal atom from group IV, V or VI and X is chalcogen atom (S, Se or Te)[17–19]. The linear chain of MX₃ is parallel to the crystallographic *b*-axis, six chalcogen atoms surround one metal atom. MX₃ bulk materials are wire-like crystals while the counterparts with few layers are nanoribbons with a quasi-1D structure. Previous works have shown that MX₃ enjoy strong in-plane optical and electrical anisotropy properties, due to their structural anisotropy[20, 21].

Nowadays, most polarization sensitive photodetectors that are composed of an optical medium with polarization effect have realized a high extinction ratio through the polarization selection of plasmon microcavities[22]. However, these polarized photodetectors suffer from several challenges, including complicated fabrication process and high cost. Recently, active materials for polarized photodetector have focused on

semiconductors with low symmetry structure[23–25], such as black phosphorus[26], TiS₃[20], GeAs[27], GeSe[28]. This work is conducive to the development of polarized photodetectors towards miniaturization and integration. Analogously, quasi-1D ZrSe₃ with low-symmetry is an ideal candidate for polarized photodetectors.

In this work, we prepared high-quality ZrSe₃ nanowires using the chemical vapor transport (CVT) method. The anisotropic optical and optoelectrical properties of ZrSe₃ are confirmed by polarization-resolved optical microscopy (PROM) and polarized optoelectrical measurements. The angularly resolved Raman spectra and polarized light absorption spectroscopy show that ZrSe₃ have in-plane anisotropy. Furthermore, the results of the polarized photodetection imply that ZrSe₃-based photodetectors are sensitive to linearly polarized light.

2. Results and discussion

2.1. Synthesis and structural analysis

High-quality ZrSe₃ nanowires (NWs) were synthesized via the CVT method. Powder Zr (0.45 g) and Se (1.35 g) were mixed in stoichiometric proportions (1 : 3) with 30 mg I₂ as transport agent. The sources were then placed in an ampoule that was placed into a double-zone furnace. The temperatures of the high temperature zone and the low temperature zone are set as 650 ℃ and 500 ℃, respectively. The ampoule was heated to 650 ℃/500 ℃ for 24 hours and kept at this temperature for 3 days. After heating, the furnace was cooled to room temperature in 1 day and the ZrSe₃ NWs had collected on the inner surface of tube. The structure of ZrSe₃ belongs to monoclinic structure with *a* = 3.788 Å, *b* = 5.485 Å and *c* = 10.156 Å, and a symmetry space group of p2₁/m[29]. Transmission electron microscopy (TEM) is an effective meth-
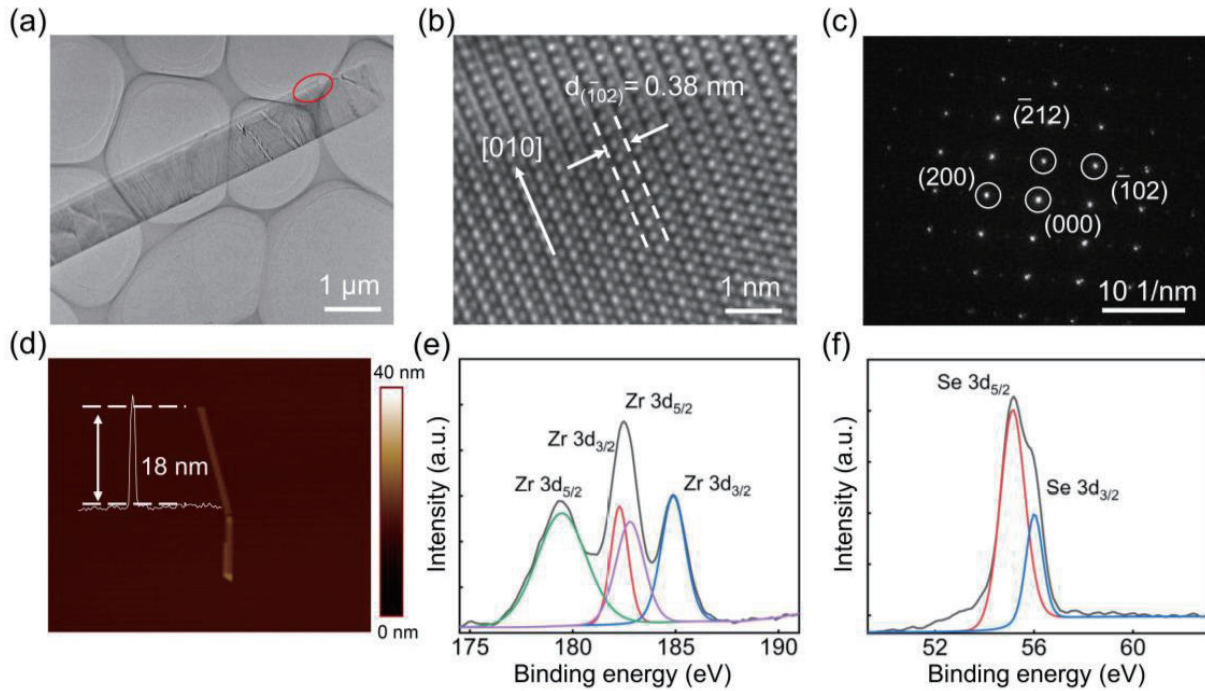
Fig. 1. (Color online) Characterization of ZrSe$_3$ crystal. (a) Low-magnification transmission electron microscopy (TEM) of the quasi-1D ZrSe$_3$. (b) High-resolution transmission electron microscopy (HRTEM) image of the quasi-1D ZrSe$_3$. (c) Selected area electron diffraction (SAED) pattern of the quasi-1D ZrSe. (d) The AFM image of ZrSe$_3$ crystal. (e) High-resolution spectra of Zr 3d core level. (f) High-resolution spectra of Se 3d core level.

od to characterize crystal microstructure and growth direction. Fig. 1(a) is a low-magnification TEM image of the ZrSe$_3$ NWs. The high-resolution transmission electron microscopy (HRTEM) image (Fig. 1(b)) was obtained from the marked region of Fig. 1(a). As shown in Fig. 1(b), the lattice spacing is 0.38 nm, which represents ($\bar{1}$02) plane, which indicates that the ZrSe$_3$ NWs prefer to grow along the *b*-axis. The obvious diffraction spots in the selected area electron diffraction (SAED) pattern (Fig. 1(c)) indicate that the ZrSe$_3$ is a single crystal. The diffraction spots agree with (200), ($\bar{1}$02) and ($\bar{2}$12) plane, respectively. The elements of Zr and Se are distributed uniformly on the nanowire, as shown in elemental mapping (Fig. S1). The energy-dispersive X-ray spectroscopy (EDX) shows that the elemental stoichiometric ratio is around 1 : 3 (Fig. S2). In addition, the ZrSe$_3$ NWs were measured by atomic force microscopy (AFM) (Fig. 1(d)), which shows that the thicknesses of ZrSe$_3$ are about 18 nm. The chemical state can be characterized through the method of X-ray photoelectron spectroscopy (XPS). As shown in Figs. 1(e) and 1(f), the binding energies of 179.48 and 182.78 eV are Zr 3d$_{5/2}$, 182.28 and 184.88 eV are Zr 3d$_{3/2}$[30]. This observation is similar with the analysis of HfTe$_3$, in which the Hf was assumed with mixed-valence states[31]. Therefore, we also speculate that Zr^{4+} (the doublets located at 182.78 and 184.88 eV) and Zr^{2+} (the doublets located at 179.48 and 182.28 eV) coexist in the ZrSe$_3$ NWs. The peak area shows that the ratio of Zr^{4+} and Zr^{2+} is approximately 1 : 1.

Angle-resolved polarized Raman spectroscopy (ARPRS) is a powerful method to characterize the material structure that can be used to determine the symmetry of chemical bond vibration[32]. The unit cell of ZrSe$_3$ includes eight atoms, giving rise to 24 normal vibration modes. The irreducible representations at the center of Brillouin zone: $\Gamma = 8A_g + 4B_g + 4A_u + 8B_u$.

Among these 24 formula units, A$_g$ and B$_g$ modes are Raman active while A$_u$ and B$_u$ are infrared-active. Fig. 2(a) shows the Raman spectra of ZrSe$_3$ NWs under 532 nm. It is clear that there are four peaks of normal Raman spectra at or near 107.22, 178.87, 234.61 and 301.4 cm^{-1}, which are all assigned to A$_g$ mode[29]. Furthermore, the polarized Raman spectra was measured in parallel and cross configurations and the ZrSe$_3$ NW was rotated from 0° to 180°. The contour color maps in Fig. 2(b) and 2(c) show the obvious anisotropy of chemical bond vibration. The typical Raman peaks of 178.9, 234.61 and 301.4 cm^{-1} are extracted and fitted in polar coordinates (Figs. 2(d) and 2(e), Fig. S3). The formula of the fitting curve can be expressed as $I \propto [e_i Re_s]^2$, where e_i and e_s are the polarization vectors of incident light and scattered light, respectively ($e_i = [\cos\theta \ \sin\theta \ 0]$, $e_{s//} = [\cos\theta \ \sin\theta \ 0]^T$, $e_{s\perp} = [-\sin\theta \ \cos\theta \ 0]^T$), and R is the Raman tensor. The Raman tensor of A$_g$ (ZrSe$_3$ correspond to symmetry space group of p2$_1$/m) is as follows:

$$A_g = \begin{bmatrix} ae^{i\cdot\varphi a} & 0 & de^{i\cdot\varphi d} \\ 0 & be^{i\cdot\varphi b} & 0 \\ de^{i\cdot\varphi d} & 0 & ce^{i\cdot\varphi c} \end{bmatrix}.$$

After calculation, the Raman scattering intensities of A$_g$ mode can be expressed as follows:

$$A_{g//} = A\cos^4\theta + B\sin^4\theta + C\sin^2 2\theta,$$

$$A_{g\perp} = A\cos^2 2\theta + B\sin^2 2\theta + C\sin 4\theta.$$

The fitting curves of cross configuration show four-leaf shapes. For parallel configuration, the fitting curves show spindle shapes. All of these results indicate that the structure
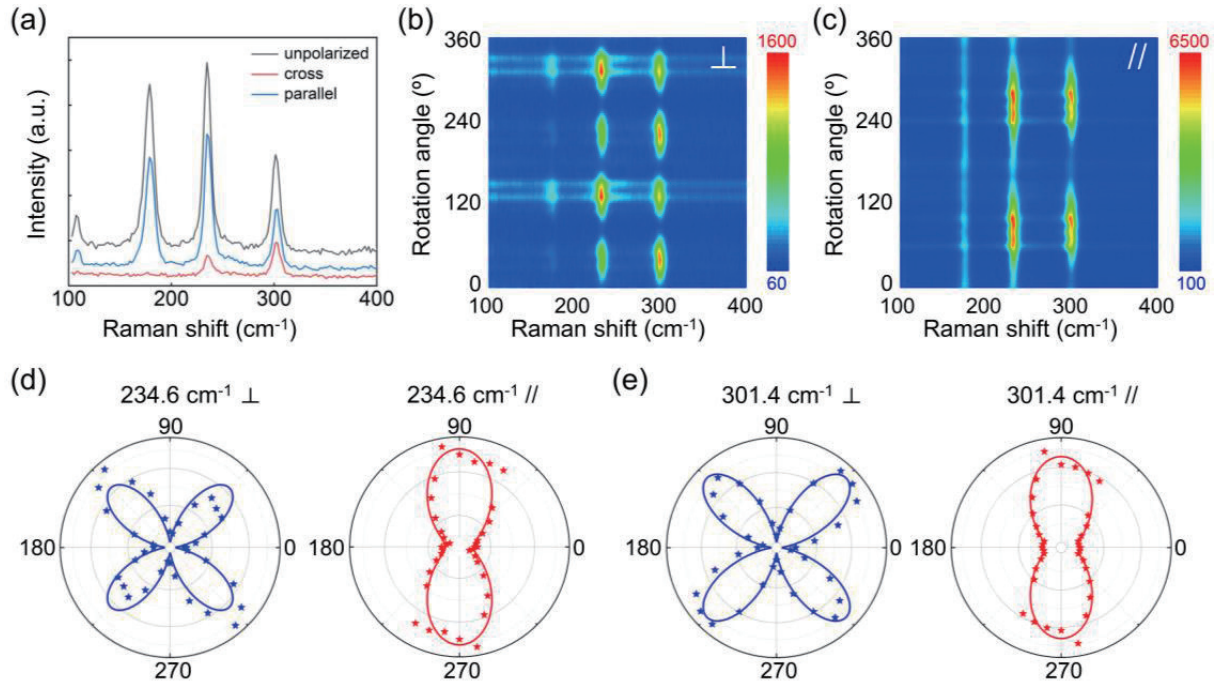
Fig. 2. (Color online) (a) Raman spectra under unpolarized and polarized laser (532 nm). (b) Counter maps of angle-resolved Raman spectra under cross configuration. (c) Counter maps of angle-resolved Raman spectra under parallel configuration. (d) Polar plots of angle-resolved and fitted peak intensities of 234.6 cm^{-1}. (e) Polar plots of angle-resolved and fitted peak intensities of 301.4 cm^{-1}.

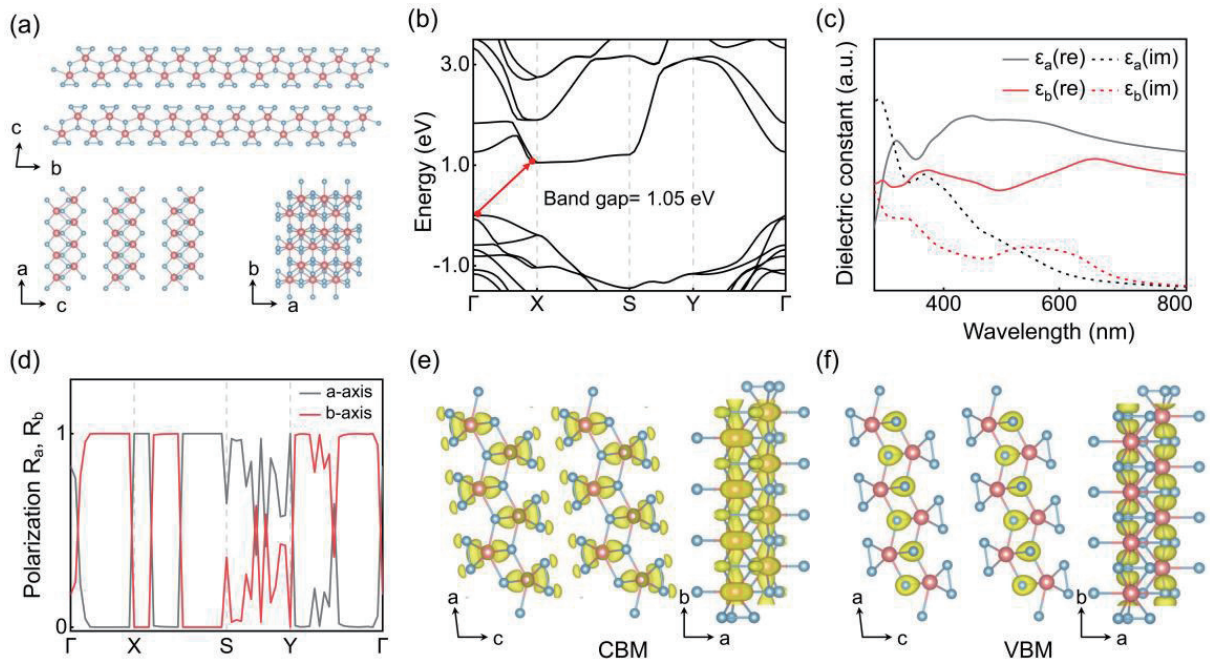Fig. 3. (Color online) (a) Atomic structure of ZrSe$_3$ crystal. (b) Band structure of layered ZrSe$_3$. (c) Calculated real parts and imaginary parts of the dielectric constant along a-axis and b-axis. (d) The R_a and R_b of optical transition $|v> \rightarrow |c>$ along the k-points path. (e, f) Partial charge density of ZrSe$_3$ at the state of CBM and VBM respectively.

of ZrSe$_3$ crystal is anisotropic.

2.2. Theoretical calculations

The schematic crystal structure in Fig. 3(a) shows infinite ribbons stacked along the b-axis and the layers are combined with each other through van der Waals interaction. Based on the crystal structure, the theoretical calculation of ZrSe$_3$ is studied. The band structure of ZrSe$_3$ was calculated through Heyd-Scuseria-Ernzerhof hybrid function method (HSE06)[33], exhibiting a band gap of 1.05 eV (Fig. 3(b)). For

the theoretical calculation, the generalized gradient approximation PBE (GGA-PBE) of correlation functional and exchange were used in the calculation[34, 35]. We then used the hybrid functional (HSE06) method for the accurate calculation of optical property and electronic structure, in which the hybrid functional was mixed with 25% exact Hartree–Fock (HF) exchange[33]. In addition, a Monkhorst-Pack k–mesh of $6 \times 9 \times 4$ sampling in the full Brillouin zone was used in the calculations[36]. The integral path of the band structure is $\Gamma \rightarrow X \rightarrow S \rightarrow Y \rightarrow \Gamma$. The electronic band structure indicates
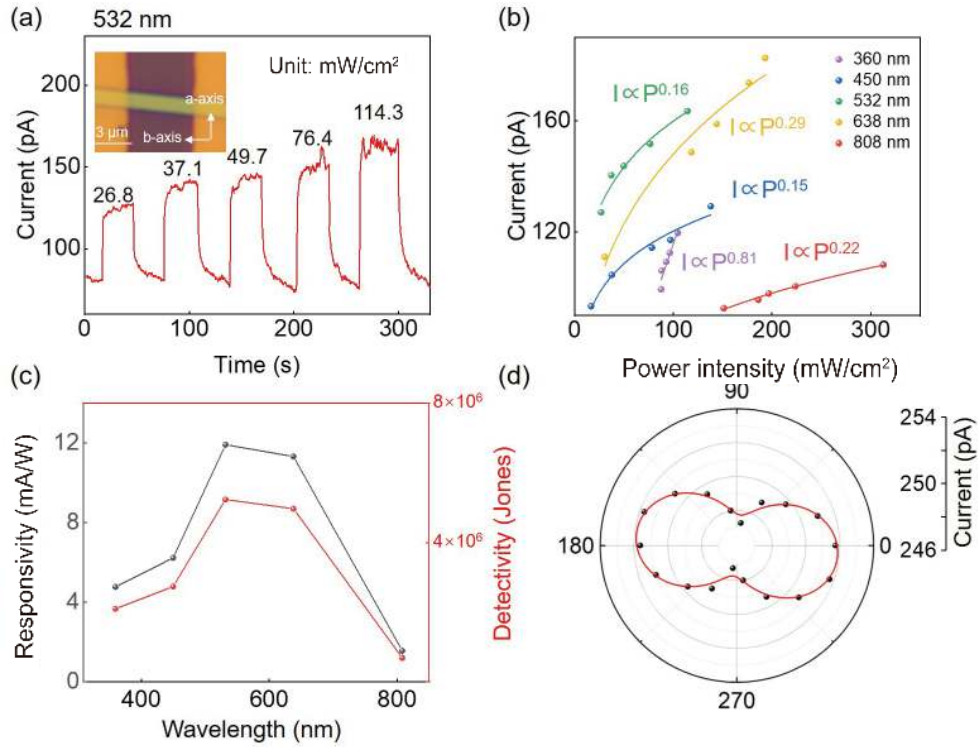
X G Wang et al.: Polarization sensitive photodetector based on quasi-1D ZrSe$_3$

Fig. 4. (Color online) (a) Time-resolved photoresponse of the ZrSe$_3$-based photodetector for a bias voltage of 5 V under 532 nm with different light power density. (b) Dependence of the photocurrent on the intensity of incident laser power. (c) The spectral responsivity and detectivity of ZrSe$_3$-based photodetector. (d) Evolution of the photocurrent with a polarized angle under 532 nm.

that the valence band maximum (VBM) is located at the X point and the conduction band minimum (CBM) is located at the Γ point. Moreover, the total density of states (DOS) and partial density of states (PDOS) (Fig. S4(a)) were calculated. It is shown that the top of the valence band is mainly composed of Se's p orbital of Se atom, while the bottom of the conduction band is mainly made up by Zr's d orbital of the Zr atom. The dielectric constants along the a-axis and b-axis of ZrSe$_3$ were calculated as shown in Fig. 3(c), and the corresponding optical absorbance coefficient (Fig. S4(b)) was calculated theoretically based on the dielectric function[37]. These results show that there is an obvious difference along a-axis and b-axis from 250 to 820 nm. The electric dipole transition probability R is positively related to the electron-radiation interaction $|<c|HeR|v>|^2$, where HeR is Hamiltonian matrix element, $|c>$ and $|v>$ are wave functions of conduction band and valence band[38]. The transition probability (R_a, R_b) from valence band maximum (VBM) to conduction band minimum (CBM) along different k-points path can be calculated through $R_a = |<c|HeR_a|v>|^2/(|<c|HeR_a|v>|^2 + |<c|HeR_b|v>|^2)$, $R_b = |<c|HeR_b|v>|^2/(|<c|HeR_a|v>|^2 + |<c|HeR_b|v>|^2)$. The results of R_a and R_b are shown in Fig. 3(d). Some typical point, such as S and Y, are selected to be analyzed. For the S point, the probability R_a is around 0.64 and R_b is around 0.36, which means that the strength of absorption along a-axis is larger than the b-axis. While for the Y point, R_a is very close to 1, which means that around the Y point the absorption only occurred along the a-axis. The difference strengths of absorption along the a-axis and b-axis lead to the polarization sensitive of ZrSe$_3$. Furthermore, the polarization sensitivity of ZrSe$_3$ is influenced by the electron transition of different energy levels and is not limited to the VBM and CBM. This obvious difference of transition probability is based on the charge dens-

ity distribution along a and b axes (Figs. 3(e)–3(f)). These results indicate that quasi-1D ZrSe$_3$ enjoys optical and optoelectric anisotropy.

2.3. Optical and photoelectrical anisotropy

The optical anisotropy of quasi-1D ZrSe$_3$ was studied through polarization-resolved optical microscopy (PROM). For the PROM test, ZrSe$_3$ NWs were exfoliated on the SiO$_2$/Si substrate, which is isotropic. During the investigation, the direction of polarization analyzer is perpendicular to the linear polarized incident light. It can be seen in Fig. S5 that the images of PROM, which are selected from 0° to 165° by a step of 15° and the brightness of ZrSe$_3$ express obvious light and dark changes. The reason for this phenomenon is that linearly polarized incident light may be refracted into two components with different vibration directions after passing through the birefringent material[39]. The result of PROM indicates that quasi-1D ZrSe$_3$ crystal enjoys obvious anisotropy.

To verify the in-plane optical anisotropy of quasi-1D ZrSe$_3$, we exfoliated and transferred the ZrSe$_3$ crystal onto mica. The measured polarization-resolved absorption spectrum is shown in Fig. S6. It is obvious that the maximum absorption appears in the polarized light of 90°, which corresponds to the a-axis. This happens because the incoming photons more effectively interact with the a-axis[40]. The absorption range covers the entire visible region and part of the near-infrared region, which is nearly coincident with the calculated absorption spectra. To investigate the photoelectric properties of quasi-1D ZrSe$_3$, the few-layers ZrSe$_3$ nanowires with a thickness of 18 nm were exfoliated and transferred onto the SiO$_2$/Si substrate (the thickness of SiO$_2$ is 300 nm). Because the polarized absorption covered from visible to near-infrared range (360–860 nm), some typical
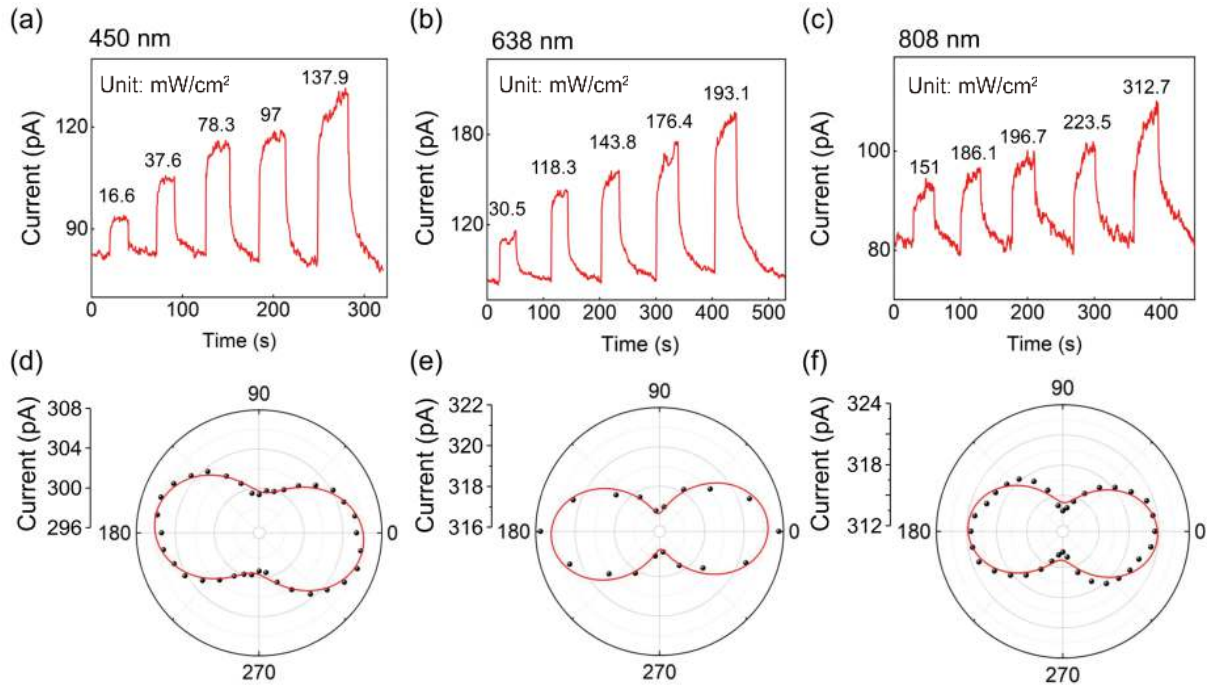
Fig. 5. (Color online) (a–c) Time-resolved photoresponse of the ZrSe$_3$-based photodetector for a bias voltage of 5 V under 450, 638 and 808 nm with different light power density respectively. (d–f) Evolution of the photocurrent with polarized angles under 450, 638 and 808 nm, respectively.

wavelengths (360, 450, 532, 638 and 808 nm) were chosen for the photodetection. As shown in Fig. 4(a), Figs. 5(a)–5(c) and Fig. S7, the photocurrent increases with the increase of the light power intensity. Specifically, under 532 nm lumination, the photocurrent increases from 127 to 166.5 pA at V_{ds} = 5 V with light power intensity from 26.8 to 114.3 mW/cm^2 (Fig. 4(a)). The relationship of photocurrent and light power intenstiy can be expressed as: $I = aP^\beta$, where a, β are dimensionless constants and I is photocurrent and P is light power intensity. Under the light irradiation, the photocurrent tends to be saturated with stronger light power intensity, which is related to the fact that carriers could be recombianted under the strong irradiation. The results after fitting are shown in Fig. 4(b). Corelatively, $\beta = 0.81, 0.15, 0.16, 0.29$ and 0.22 corresponding to 360, 450, 532, 638 and 808 nm, respectively. In addition, the other two parameters of the photodetectors are responsivity (R) and detectivity (D^*). Responsivity indicates the ability of photodetectors to convert a light signal into an electrical signal, which can be expressed as: $R = \Delta I/(P_\lambda S)$, where ΔI is the difference of photocurrent and dark current, P_λ is power intensity of incident light and S is the effective area of photodetectors. Detectivity (R^*) reflects the sensitivity for perceiving weak light, which can be demonstrated as $D^* = RS^{1/2}/(2eI_d)^{1/2}$, where R is the responsivity, e is unit charge and I_d is dark current. As shown in Fig. 4(c), the photodetector based on ZrSe$_3$ has good performance in the ultraviolet and near-infrared region, especially R and D^* reach 11.9 mA/W and around 10^6 Jones at 532 nm. This happens because the short wavelength laser can excite more electrons that are located at different valence bands to the conduction band. The decrease in the ultraviolet region is due to the increased recombination rate of the carriers. As shown in Fig. S8, I–V curves of ZrSe$_3$-based photodetectors at 360, 450, 638 and 808 nm indicate that the metal-semiconductor contact is

an Ohmic contact. Moreover, the rise time is the time from 10% saturated photocurrent to 90% saturated photocurrent and the decay time is the time from 90% saturated photocurrent to 10% saturated photocurrent. The rise time of ZrSe$_3$-based photodetector is around 2.8 s, while for decay time it is about 30 s. The decay time of ZrSe$_3$-based photodetector is longer than the rise time because the surface defect states of ZrSe$_3$ prolong the recombination process of the photogenerated electric-hole pairs. In addition, the short wavelength laser, with larger photon energy, has a higher coupling efficiency leading to thermal heating effect, which results in prolonged response time. The influence of the width of the device is also discussed. The photoelectrical performance of photodetector with different widths (0.7, 1.2, 1.8 μm) is measured. The results (Fig. S9) show that the ZrSe$_3$-based photodetector with appropriate width (1.2 μm) has better photoelectrical properties.

Raman spectra, PROM and absorption spectra show that ZrSe$_3$ NWs possess an obvious crystal structure and optical anisotropy. These results prompt us to expend the investigation from photoelectric detection to polarized photodetection. The linearly polarized light was obtained through the assistance of Glan-Taylor prism, which acts as a polarizer. In addition, we used the half-wave plate to change the direction of the linearly polarized light. The extinction ratio of polarizer (Glan-Taylor prism) reaches 10^5 : 1, which guarantees the appearance of the linearly polarized light. The drain–source voltage was fitted at 5 V, the direction of linearly polarized light was rotated with a step of 10° or 20°. The photocurrents with the polarized angle from 0° to 360° were extracted and plotted in polar coordinate system (Fig. 4(d) and Figs. 5 (d) and 5(e)). The direction of b-axis of ZrSe$_3$ NWs was defined as 0°. They were then fitted through the equation: $I_{ph}(\theta) = I_{pha}\cos^2(\theta+\varphi)+I_{phb}\sin^2(\theta + \varphi)$, where I_{pha} and I_{phb} are the

Table 1.　Summary of the performance of a device based on quasi-1D ZrSe$_3$.

Wavelength (nm)	Optical power density (mW/cm^2)	Responsivity (mA/W)	I_{max}/I_{min}
360	150	4.8	–
450	150	6.2	1.02
532	150	11.9	1.03
638	150	11.3	1.02
808	150	1.6	1.1

photocurrents along *a*-axis and *b*-axis of ZrSe$_3$ NWs, θ is the polarization angle[41]. The gourd-shaped fitting curves indicate that the ZrSe$_3$-based photodetector enjoys polarization-sensitivity and the largest photocurrents are all reached along the *a*-axis of ZrSe$_3$ crystal. The I_{pha}/I_{phb} ratios at 450, 532, 638 and 808 nm are 1.02, 1.03, 1.02 and 1.1, respectively. The optoelectrical properties of ZrSe$_3$-based photodetector are summarized in Table 1. This shows that the quasi-1D ZrSe$_3$ crystal has application value in the field of optoelectronics.

3. Conclusion

In summary, layered quasi-1D nanowires ZrSe$_3$ were synthesized with the CVT method. The HRTEM, APRPS, PROM, absorption spectroscopy and polarized optoelectronic investigations show the anisotropy of ZrSe$_3$ NWs. The ZrSe$_3$-based photodetector performs a wide photoresponse from UV to NIR with impressive optoelectronic properties, with photoresponsivity of 11.9 mA/W and detectivity of ~10^6 at 532 nm. It also exhibits polarization-sensitivity due to the anisotropic structure. These results show that quasi-1D ZrSe$_3$ NWs have the potential in application of polarization photodetector without the help of optical polarizer.

Acknowledgements

Appendix A. Supplementary materials

Supplementary materials to this article can be found online at https://doi.org/10.1088/1674-4926/43/10/102001.

References

[1] Radisavljevic B, Radenovic A, Brivio J, et al. Single-layer MoS$_2$ transistors. Nat Nanotechnol, 2011, 6, 147
[2] Patra A, Rout C S. Anisotropic quasi-one-dimensional layered transition-metal trichalcogenides: Synthesis, properties and applications. RSC Adv, 2020, 10, 36413
[3] Cui Q N, Lipatov A, Wilt J S, et al. Time-resolved measurements of photocarrier dynamics in TiS$_3$ nanoribbons. ACS Appl Mater Interfaces, 2016, 8, 18334
[4] Ferrer I J, Ares J R, Clamagirand J M, et al. Optical properties of titanium trisulphide (TiS$_3$) thin films. Thin Solid Films, 2013, 535, 398
[5] Ferrer I J, Maciá M D, Carcelén V, et al. On the photoelectrochemical properties of TiS$_3$ films. Energy Procedia, 2012, 22, 48
[6] Gilbert S J, Lipatov A, Yost A J, et al. The electronic properties of Au and Pt metal contacts on quasi-one-dimensional layered TiS$_3$(001). Appl Phys Lett, 2019, 114, 101604
[7] Island J O, Buscema M, Barawi M, et al. Ultrahigh photoresponse of few-layer TiS$_3$ nanoribbon transistors. Adv Opt Mater, 2014, 2, 641
[8] Papadopoulos N, Frisenda R, Biele R, et al. Large birefringence and linear dichroism in TiS$_3$ nanosheets. Nanoscale, 2018, 10, 12424
[9] Pant A, Torun E, Chen B, et al. Strong dichroic emission in the pseudo one dimensional material ZrS$_3$. Nanoscale, 2016, 8, 16259
[10] Xiao Y, Zhou M Y, Liu J L, et al. Phase engineering of two-dimensional transition metal dichalcogenides. Sci China Mater, 2019, 62, 759
[11] Huang H, Gao M, Wang J H, et al. Intercalator-assisted plasma-liquid technology: An efficient exfoliation method for few-layer two-dimensional materials. Sci China Mater, 2020, 63, 2079
[12] Huang Y L, Chen W, Wee A T S. Two-dimensional magnetic transition metal chalcogenides. SmartMat, 2021, 2, 139
[13] Zhang Z C, Zhao B, Shen D Y, et al. Synthesis of ultrathin 2D non-layered α-MnSe nanosheets, MnSe/WS$_2$ heterojunction for high-performance photodetectors. Small Struct, 2021, 2, 2100028
[14] Han X, Xu Z S, Wu W Q, et al. Recent progress in optoelectronic synapses for artificial visual-perception system. Small Struct, 2020, 1, 2000029
[15] Tian X Y, Liu Y S. Van der Waals heterojunction ReSe$_2$/WSe$_2$ polarization-resolved photodetector. J Semicond, 2021, 42, 032001
[16] Fang H H, Hu W D. Hybrid heterojunctions based on 2D materials and 3D thin-films for high-performance photodetectors. Sci China Phys Mech Astron, 2017, 60, 027031
[17] Iyikanat F, Senger R T, Peeters F M, et al. Quantum-transport characteristics of a p-n junction on single-layer TiS$_3$. Chemphyschem, 2016, 17, 3985
[18] Sun R, Gu Y, Yang G F, et al. Theoretical study on the interfacial properties of monolayer TiS$_3$-metal contacts for electronic device applications. J Phys Chem C, 2019, 123, 7390
[19] Kang J, Wang L W. Robust band gap of TiS$_3$ nanofilms. Phys Chem Chem Phys, 2016, 18, 14805
[20] Liu S J, Xiao W B, Zhong M Z, et al. Highly polarization sensitive photodetectors based on quasi-1D titanium trisulfide (TiS$_3$). Nanotechnology, 2018, 29, 184002
[21] Wang X T, Wu K D, Blei M, et al. Highly polarized photoelectrical response in vdW ZrS$_3$ nanoribbons. Adv Electron Mater, 2019, 5, 1900419
[22] Li L, Xiong D Y, Wen J, et al. A surface plasmonic coupled mid-long-infrared two-color quantum cascade detector. Infrared Phys Technol, 2016, 79, 45
[23] Gao J, Zheng Y, Yu W, et al. Intrinsic polarization coupling in 2D α-In$_2$Se$_3$ toward artificial synapse with multimode operations. SmartMat, 2021, 2, 88
[24] Zhou Z Q, Cui Y, Tan P H, et al. Optical and electrical properties of two-dimensional anisotropic materials. J Semicond, 2019, 40, 061001
[25] Fang J Z, Zhou Z Q, Xiao M Q, et al. Recent advances in low-dimensional semiconductor nanomaterials and their applications in high-performance photodetectors. InfoMat, 2020, 2, 291
[26] Long M S, Gao A Y, Wang P, et al. Room temperature high-detectivity mid-infrared photodetectors based on black arsenic phosphorus. Sci Adv, 2017, 3, e1700589
[27] Zhou Z Q, Long M S, Pan L F, et al. Perpendicular optical reversal of the linear dichroism and polarized photodetection in 2D GeAs. ACS Nano, 2018, 12, 12416
[28] Wang X T, Li Y T, Huang L, et al. Short-wave near-infrared linear dichroism of two-dimensional germanium selenide. J Am Chem Soc, 2017, 139, 14976

[29] Osada K, Bae S, Tanaka M, et al. Phonon properties of few-layer crystals of quasi-one-dimensional ZrS_3 and $ZrSe_3$. J Phys Chem C, 2016, 120, 4653

[30] Yu X, Wen X K, Zhang W F, et al. Fast and controlled growth of two-dimensional layered $ZrTe_3$ nanoribbons by chemical vapor deposition. CrystEngComm, 2019, 21, 5586

[31] Li J, Peng J, Zhang S, et al. Anisotropic multichain nature and filamentary superconductivity in the charge density wave system $HfTe_3$. Phys Rev B, 2017, 96, 174510

[32] Wu J X, Mao N N, Xie L M, et al. Identifying the crystalline orientation of black phosphorus using angle-resolved polarized Raman spectroscopy. Angew Chem Int Ed, 2015, 54, 2366

[33] Heyd J, Scuseria G E, Ernzerhof M. Hybrid functionals based on a screened Coulomb potential. J Chem Phys, 2003, 118, 8207

[34] Perdew J P, Burke K, Wang Y. Generalized gradient approximation for the exchange-correlation hole of a many-electron system. Phys Rev B, 1996, 54, 16533

[35] Perdew J P, Burke K, Ernzerhof M. Generalized gradient approximation made simple. Phys Rev Lett, 1996, 77, 3865

[36] Monkhorst H J, Pack J D. Special points for Brillouin-zone integrations. Phys Rev B, 1976, 13, 5188

[37] Saha S, Sinha T P, Mookerjee A. Electronic structure, chemical bonding, and optical properties of paraelectric $BaTiO_3$. Phys Rev B, 2000, 62, 8828

[38] Zhao K, Yang J H, Zhong M Z, et al. Direct polarimetric image sensor and wide spectral response based on quasi-1D Sb_2S_3 nanowire. Adv Funct Mater, 2021, 31, 2006601

[39] Hou S J, Guo Z F, Yang J H, et al. Birefringence and dichroism in quasi-1D transition metal trichalcogenides: Direct experimental investigation. Small, 2021, 17, e2100457

[40] Yang H, Pan L F, Wang X T, et al. Mixed-valence-driven quasi-1D $Sn^{II}Sn^{IV}S_3$ with highly polarization-sensitive UV-vis-NIR photoresponse. Adv Funct Mater, 2019, 29, 1904416

[41] Xiao M Q, Yang H, Shen W F, et al. Polarization-sensitive photodetectors: Symmetry-reduction enhanced polarization-sensitive photodetection in core-shell SbI_3/Sb_2O_3 van der Waals heterostructure. Small, 2020, 16, 2070036

Xingang Wang received his B.S. degree in 2018 from Qingdao University. He is currently a Ph.D. candidate in physical electronics from the Institute of Semiconductors, Chinese Academacy of Sciences (CAS), Beijing China, under the supervision of Prof. Jianguo Liu. His research focuses on the electronic, photoelectric properties of 2D layered materials and high sensitivity photodetector devices.

Zeping Zhao got her B.S. degree from Hebei University of Technology, Tianjin, China, in 2014, and received a Ph.D. degree in physical electronics from the Institute of Semiconductors, Chinese Academy of Sciences (CAS), Beijing, China, in 2019. Now she is working for the Institute of Semiconductors, CAS. She has published more than 20 articles in scientific journals. Her study interests focus on high-frequency photodetector devices, optical fiber communication systems technology, high-speed microwave package design, and array hybrid integration.

Jianguo Liu got his B.S. degree in Inner Mongolia Normal University, Inner Mongolia, China, in 1998, received a master's degree from the Anhui Institute of Optics and Fine Mechanics, Chinese Academy of Sciences (CAS), Anhui, China, in 2004, and got his Ph.D. degree from Nankai University, Tianjin, China, 2007. He worked at Northwestern University as a postdoctoral fellow, America, from 2010 to 2011. Now he is a research fellow of the Institute of Semiconductors, CAS. And he is also a professor of CAS. He has published more than 100 articles in scientific journals and got 67 patents for invention. His research focuses on applied optics. Dr. Liu received the funding of the National Science Fund for Outstanding Youth in 2017.

Zhongming Wei received his B.S. from Wuhan University (China) in 2005, and Ph.D. from the Institute of Chemistry, Chinese Academy of Sciences in 2010 under the supervision of Prof. Daoben Zhu and Prof. Wei Xu. From August 2010 to January 2015, he worked as a postdoctoral fellow and then Assistant Professor in Prof. Thomas Bjørnholm's group at University of Copenhagen, Denmark. Currently, he is working as a Professor at the Institute of Semiconductors, Chinese Academy of Sciences. His research interests include low-dimensional semiconductors and their optoelectronic devices.